OPTICA

Electric-field-resolved near-infrared microscopy

Mikhail Mamaikin,[1,2] **Yik-Long Li,**[1,2] **Enrico Ridente,**[1,2] **Wei Ting Chen,**[3]
Joon-Suh Park,[3,4] **Alexander Y. Zhu,**[3] **Federico Capasso,**[3] **Matthew Weidman,**[1,2]
Martin Schultze,[1,5] **Ferenc Krausz,**[1,2] **and Nicholas Karpowicz**[1,6,*]

[1]*Max-Planck-Institut für Quantenoptik, Hans-Kopfermann-Strasse 1, 85748 Garching, Germany*
[2]*Fakultät für Physik, Ludwig-Maximilians-Universität, Am Coulombwall 1, 85748 Garching, Germany*
[3]*Harvard John A. Paulson School of Engineering and Applied Sciences, Harvard University, Cambridge, Massachusetts 02134, USA*
[4]*Nanophotonics Research Center, Korea Institute of Science and Technology (KIST), Seoul 02792, Republic of Korea*
[5]*Institute of Experimental Physics, Graz University of Technology, Graz, Austria*
[6]*CNR NANOTEC Institute of Nanotechnology, via Monteroni, 73100 Lecce, Italy*
Corresponding author: nicholas.karpowicz@mpq.mpg.de

Access to the complete spatiotemporal response of matter due to structured light requires field sampling techniques with sub-wavelength resolution in time and space. We demonstrate spatially resolved electro-optic sampling of near-infrared waveforms, providing a versatile platform for the direct measurement of electric field dynamics produced by photonic devices and sub-wavelength structures both in the far and near fields. This approach offers high-resolution, time- or frequency-resolved imaging by encoding a broadband signal into a narrowband blueshifted image, lifting the resolution limits imposed by both chromatic aberration and diffraction. Specifically, measuring the field of a near-infrared laser with a broadband sampling laser, we achieve 1.2 μm resolution in space and 2.2 fs resolution in time. This provides an essential diagnostic for complete spatiotemporal control of light with metasurface components, demonstrated via a metalens as well as a meta-axicon that forms broadband, ultrashort, truncated Bessel beams in the near infrared. Finally, we demonstrate the electric field dynamics of locally enhanced hot spots with sub-wavelength dimensions, recording the full temporal evolution of the electric field at each point in the image simultaneously. The imaging modality opens a path toward hyperspectral microscopy with simultaneous sub-wavelength resolution and wide-field imaging capability. © 2022 Optica Publishing Group under the terms of the Optica Open Access Publishing Agreement

https://doi.org/10.1364/OPTICA.454562

1. INTRODUCTION

The time-dependent electric field of light contains rich information; however, only a small portion of the information, mainly intensity, is accessed by conventional imaging systems. Accessing the remaining information in the visible or near-infrared region is a fascinating challenge: full electric field imaging, or its Fourier-domain counterpart of phase-resolved hyperspectral imaging. Such an imaging technique could identify, for example, the spatiotemporal electric field dynamics in a photonic device or enable new approaches to label-free microscopy.

Although its utility is well known in the microwave [1] and terahertz [2] spectral ranges, access to the temporal structure of electric fields in near infrared and visible is a challenging task. It has only recently been realized through attosecond techniques based on extreme nonlinear optical effects taking place in gases, including the production and application of attosecond pulses [3,4], or associated effects such as photoionization [5] and high harmonic generation [6,7]. Recent advances in attosecond pulse generation in solids [8–10] and other techniques have allowed optical field waveforms to be measured in solid-state devices [11–13]. Another technique, electro-optical sampling [14,15] (EOS), which was

only recently extended to the near infrared [16] and visible [17], offers an interesting alternative.

EOS has successfully been applied to terahertz imaging, via raster scanning [18], and in wide-field imaging geometry [19,20]. Notably, both configurations can access near-field and evanescent components of the electric field, by placing a thin electro-optic crystal underneath the object of interest [21–25] or scanning the object with a near-field probe [26–28]. In fact, wide-field, near-infrared EOS imaging has a number of properties that present not only sub-cycle-resolved temporal resolution to study light–matter interaction in sub-wavelength systems, but also a viable method of broadband microscopy with spatial resolution below the diffraction limit given by the wavelength of the field being recorded.

Here, we apply EOS imaging to the near infrared, in the range from 120 to 200 THz (2.7 to 1.5 μm). The resulting time-resolved imaging system allows for high-resolution imaging across a broad spectral range and can be used to record the full electric field waveform at each pixel of a camera. This provides a unique platform to study the electric field produced in the focus of metasurface optical components and to take a series of snapshots of the locally enhanced electric field in the vicinity of wavelength-scale metallic

structures. These examples support the demonstration of a novel microscopy in the telecom band with high resolution in time and space showing a complete spatiotemporal characterization of light fields in this technologically important spectral range. A unifying aspect of these measurements is that the electric field of light itself is the object observed with the microscope. By taking high-resolution snapshots of the electric field of an ultrashort pulse, we can see in fine detail the structures imprinted upon it resulting from its interaction with interesting optical elements and precisely locate and understand any unwanted distortions and identify interesting features over a wide field of view.

EOS imaging is based on the use of an ultrashort sampling pulse to record the electric field of a broadband infrared laser beam, the test field, inside a nonlinear crystal at a given instant. The information describing the field is encoded into the polarization state of the sampling pulse, as illustrated in Fig. 1(a). In the case of EOS of rapidly oscillating fields, the nonlinear interaction between the fields induces the emission of coherent light at the sum and difference frequencies between the field being measured and the sampling pulse. If the period of the oscillation is much longer that the sampling pulse duration, this can be ignored, and the emitted light is approximately degenerate with the original sampling pulse (e.g., in the limit of zero frequency). This amounts to an effective modification to the refractive index ellipsoid of the medium: the Pockels effect. When the frequency is higher, however, this splitting into sum and difference frequency pushes the field information to the extrema of the spectrum. The polarization vectors of spectral components of the sampling pulse at these frequencies will rotate with the same linear field dependence of the Pockels effect, if the condition is met that the nonlinearly generated light is degenerate with and polarized orthogonally to the input sampling pulse.

Isolating the proper wavelength region using a spectral filter improves the signal-to-noise ratio [25,29] of the measurement, and can be used to control its spectral response [16].

For broadband imaging, EOS and this spectral isolation have significant benefits. First, selecting the sum frequency process through phase matching and filtration [see Fig. 1(b)], the information of interest is now carried in a relatively narrow range (a few tens of nanometers) in the visible spectral range instead of approximately 1 μm bandwidth of a near-infrared laser beam, significantly reducing chromatic aberrations. This spectral compression emerges as a result of the convolution of the spectra of the sampling pulse and measured field in the three-wave mixing process taking place in the $\chi^{(2)}$ medium, as described in Supplement 1. As long as the required frequencies are present in the input sampling pulse, the amplitude and phase information is encoded into a narrowband output signal. The result is wide-field imaging with more than 100 THz detection bandwidth, practically free of chromatic aberration.

Moreover, the high spatial frequency components that were forbidden to propagate can be carried into the far field. For example, the imaging of an object, much smaller than the test-field wavelength, λ_t, can be well understood by Fourier decomposition of its scattered wave into plane wave components with a continuum of transverse wave vectors k_x and k_y. However, plane wave components such that $k_x^2 + k_y^2 > \omega^2/c^2$ cannot propagate and will
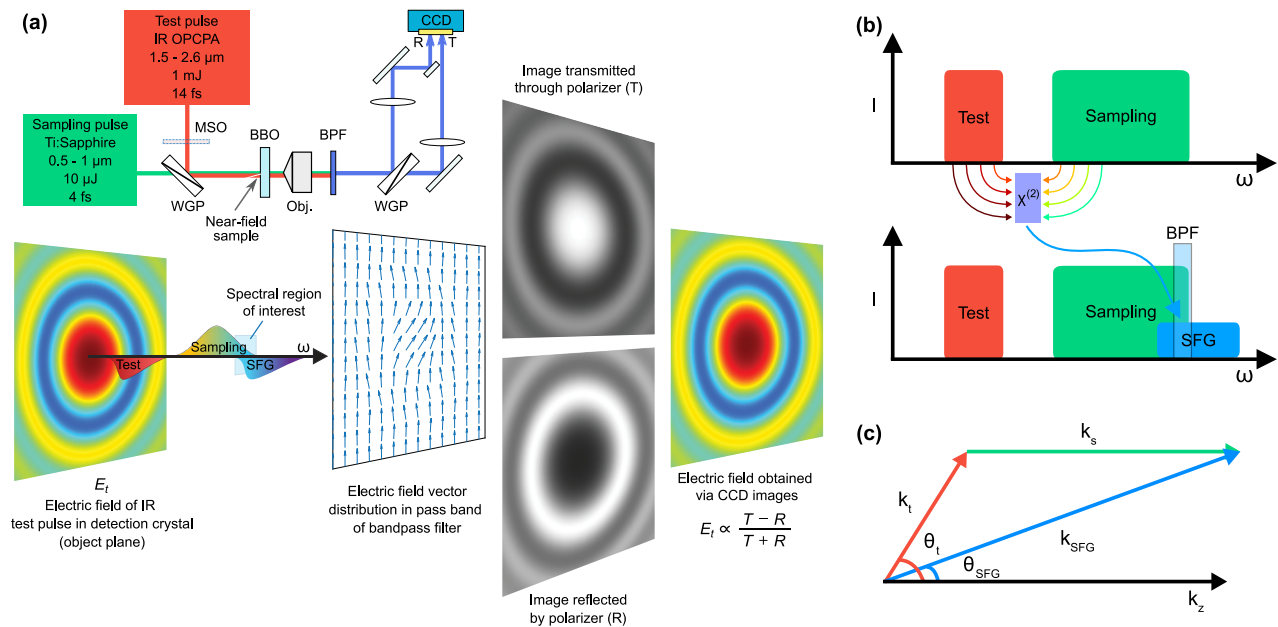
Fig. 1. Experimental concept. (a) Experimental setup wherein two synchronized laser sources provide the necessary sampling pulses and fields to be measured. The electric field distribution of the NIR wave to be recorded is focused using the metasurface optic (MSO) and coincident with a broadband sampling field with a variable relative time delay. As illustrated beneath the diagram of the system, due to the second-order optical nonlinearity in the BBO crystal, a sum frequency generation (SFG) pulse emerges, with a polarization orthogonal to the sampling pulse, and shows a partial spectral overlap with the sampling pulse spectrum. The marked area of overlap constitutes the spectral region of interest, where the electro-optic image, a scalar representation of the electric field, is encoded in the direction of the electric field vectors of the sampling pulse, which is recorded on a CCD through images transmitted and reflected by a wire-grid polarizer (WGP), after passing through a bandpass filter (BPF). (b) A schematic view of the $\chi^{(2)}$ mixing process, to produce a high-frequency signal from the convolution of the spectra of the test and sampling pulses, the result of which has a spectral overlap with the input sampling spectrum. This overlap region, which can be significantly more narrowband than either the test or sampling pulse, is in the passband of the BPF, producing a narrowband image which contains information describing the full range of IR frequencies present in the field under study. (c) Addition of wave vectors, k_t of the test pulse, and k_s of the sampling pulse in the SFG process leading to a reduction of numerical aperture required to reach the same spatial resolution.

decay exponentially, limiting the spatial resolution to approximately a wavelength. If, *prior* to propagation, the nonlinearity in the medium produces a new wave, with higher frequency $\omega_t + \omega_s$ (where ω_t and ω_s are the frequencies of the test and sampling fields, respectively), the limit on k_x and k_y is lifted significantly. Illustrated in Fig. 1(c), this allows wide-field NIR imaging with sub-wavelength resolution as the information of the infrared light transfers to the sum frequency generation (SFG). Accordingly, the spatial resolution is now determined by the diffraction limit given by the wavelength of the SFG: the resolution is improved by approximately the ratio of wavelength of the field being measured and the passband of the spectral filter of the detection system. The diffraction angle θ_{SFG} becomes smaller compared with θ_{IR}, leading to a significant reduction of the numerical aperture of objective required a given resolution. Diffraction correspondingly limits the resolution of the field measurement based on the wavelength of the detected spectral components of the sampling pulse, rather than the wavelength of the infrared field being recorded.

Although significant progress has been made in approaches to record the spatiotemporal structure of laser fields [30–34], this combination of high spatial and temporal resolution in the measurement of an electromagnetic field is unprecedented. With the possibility of sub-wavelength spatial resolution and sub-cycle temporal resolution, the effective volume in time and space is only 3 fs μm^2.

The ability to completely characterize fields in the near infrared is the first step in obtaining complete control over the structure of strong fields in both space and time. A first example to showcase this imaging technique is the characterization of fields produced by optical elements on the forefront of realizing this level of control: metasurface optics. The realization of metasurface optical elements [35–37] relies on the arrangement and design of nanostructures

to control the wavefront of the transmitted light. An interesting, and related pair of questions are, does the spatial control they offer compromise the time-domain properties of broadband radiation, and could they offer control over the temporal properties of the electric fields? This control is closely related to the chromatic aberrations of the optical components [38–40]: wavelength-dependent phase shifts of nanostructures impart a customized phase profile to engineer the temporal distribution of the transmitted light. Correspondingly, a properly designed metasurface enables the simultaneous confinement of the light field in space and time to maximize the peak intensity in short-pulse laser irradiation.

2. SPATIOTEMPORAL ELECTRIC FIELD IN THE FOCUS OF A METALENS

We first show the case of a metasurface lens (metalens) that comprises SiO_2 nanopillars of different diameters on a fused silica substrate, shown in Figs. 2(a) and 2(b) via scanning electron microscope (SEM) images [41]. This metalens exhibits a high degree of chromatic aberration [40,42]. A beta barium borate (BBO) crystal was placed at the focal plane of the metalens as the medium for EOS. The focused electric field inside the BBO crystal $E(x, y, t)$ is observed by scanning the time delay between the test and sampling laser beams. As the time delay varies, the spatially resolved polarization changes provide a snapshot of the infrared field at different moments in time. Figure 2 shows two slices of the measured three-dimensional electric field of the test pulse, $E_t(x, y, t)$: Fig. 2(c) at the focal plane for a single moment in time, i.e., $E_t(x, y, 0)$, and in Fig. 2(d), a spatiotemporal cross section, $E_t(0, y, t)$. From Fig. 2(d), one can see that the incident laser with a nominal pulse duration of 14 fs becomes about 50 fs after being focused. This is because different incident frequencies are focused to various focal
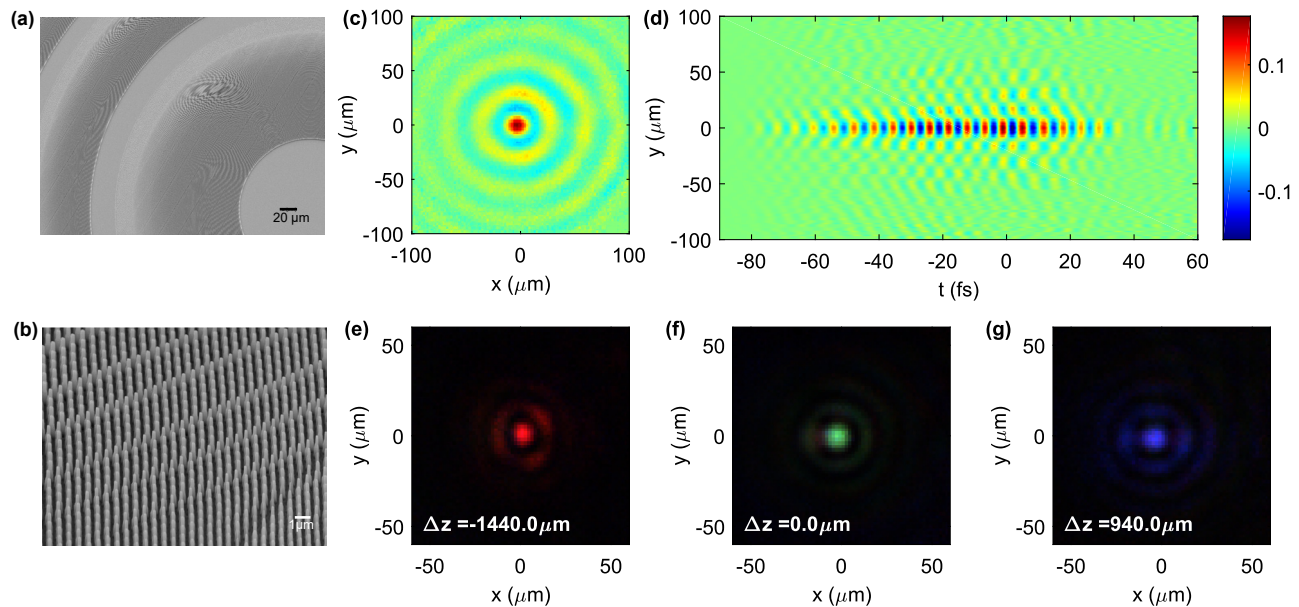
Fig. 2. Characterization of the focal spot of a chromatic metalens. (a), (b) SEM images of a metalens. The metalens has a numerical aperture of 0.13 at $\lambda = 800$ nm and consists of SiO_2 pillars of various diameters and with the same height of 2 μm. An image of higher magnification in oblique view is given in (b). (c), (d) EOS images of the focal spot of the metalens. The measurement itself forms a three-dimensional recording of electric field $E_t(x, y, t)$. These images were taken with a 4×, 0.1 NA objective. (c) Electric field pattern observed at the time-delay corresponding to the strongest electric field strength. The bullseye pattern of the wavefront shows the defocus of many spectral components of the pulse. (d) Spatiotemporal image of the electric field in the plane $E_t(x = 0, y, t)$. (e)–(g) False color images of the focus calculated at different planes from the measurement, using the availability of spectral amplitude and phase at each pixel of the image. Fourier transformation of the waveforms recorded at each pixel provides high-resolution spectra, which are then reduced to three spectral channels and mapped to color information, where red, green, and blue correspond to 145 THz, 168 THz, and 189 THz, respectively.

planes due to chromatic aberration. At a given position on the optical axis, only a subset of the bandwidth of the incident laser can interfere constructively, causing the increase of pulse duration. This is confirmed by the focal spot images at different z-planes showing a variety of frequencies, in Figs. 2(e)–2(g).

The measured electric field distribution provides a complete characterization of the amplitude and phase of the light in the plane of the BBO crystal, which, in the case of linear interaction, fully determine the form of the distribution with propagation. The spatiotemporal field in other planes can be straightforwardly calculated from this based on Fourier optics, as described in Supplement 1. Thus, the image only needs to be taken once with the crystal in a given location [Fig. 2(f)], and the images corresponding to other positions [Figs. 2(e) and 2(g)] are determined by the information already recorded. The method provides a useful characterization for correcting aberrations by backpropagating the measured electric field to the exit pupil of a lens. The images are shown in false color, remapping the broadband near-infrared field to the visible spectrum to give a more intuitive picture a portion of the hyperspectral information contained in the field measurement.

3. DIRECT FIELD MEASUREMENT OF A FEW-CYCLE BESSEL BEAM

To circumvent the aforementioned chromatic-aberration-induced pulse broadening, we, based on our previous work, designed and fabricated a metasurface axicon that shows a wavelength-independent Bessel beam profile [43]. The metasurface axicon was implemented by amorphous silicon nanofins with the same height, length, and width but of different rotations to impart upon the incident light a spatially varying phase delay according to the Pancharatnam–Berry phase [44,45]. SEM images are shown in Figs. 3(a) and 3(b). The geometric sizes of each nanofin were chosen such that at an incident wavelength of 1.5 µm, the nanofin mimics a miniature half-wave plate for maximizing efficiency.

Figures 3(c) and 3(d) show the spatiotemporal field distributions generated by the metasurface axicon and a glass axicon. These optical elements transform the incident field into a truncated Bessel beam with interesting properties, such as being nondiffracting [46] and self-reconstructing [47]. The metasurface axicon was designed such that the transverse intensity distribution is invariant with wavelength [44], resulting in a temporal profile that is both shorter in time and more consistent over the profile of the focus. Comparing Figs. 3(e) and 3(f) for the metasurface axicon and conventional glass axicon, the false color image in Fig. 3(e) shows that the Bessel beam generated by the metasurface axicon has its nodes and antinodes in consistent radial positions for all wavelengths, yielding significantly more pixels where the pulse duration reaches its ∼14 fs nominal value, as indicated by the histogram of pulse durations in Fig. 3(g). In the case of the conventional glass axicon, the Bessel beam profiles of different incident wavelengths are not identical, e.g., see the resultant color spread in the rings, leading to more positions with longer pulse duration.

4. FIELD-RESOLVED NEAR-FIELD MICROSCOPY IN THE NEAR INFRARED

The local detection of fields has recently attracted significant interest from the ultrafast community, especially the investigation of fields inside of plasmonic antennas [48,49]. We have demonstrated
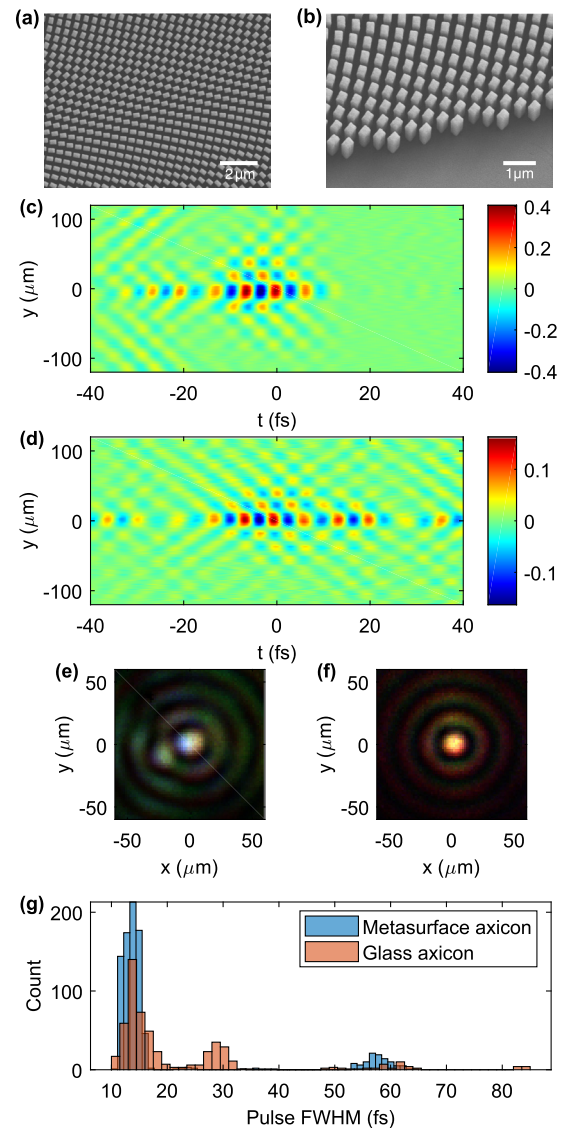
Fig. 3. Characterization of truncated Bessel beams produced by a metasurface axicon and a glass axicon. (a), (b) SEM images of a fabricated meta-axicon comprising amorphous silicon nanofins. (c) Spatiotemporal electric field distribution along the y axis of meta-axicon generated Bessel beam. The numerical aperture of this meta-axicon is about 0.06. Electric field images of the resulting beam were taken with 4×, 0.1 NA objective. (d) Spatiotemporal electric field distribution produced by a glass axicon of approximately the same numerical aperture. (e) False color image of the Bessel beam produced by the metasurface axicon, where red, green, and blue correspond to frequencies of 135 THz, 164 THz, and 192 THz, respectively. (f) False color image of the Bessel beam produced by the glass axicon. (g) Histogram of pulse durations (full width at half-maximum of intensity) produced by the two axicons.

how the far-field electric field of metalenses can be recorded. EOS imaging can reach into the near field, as well, providing a route to new insight to the physics of nanophotonics. The electric near field of objects placed directly on the detection crystal appears in the resulting image, which can be utilized to produce sub-wavelength resolution of, e.g., the electric field dynamics of small resonators [23,50,51] and could lead to broadband images of biological samples [52], so long as the target is thin enough that the near field reaches the crystal (e.g., the dendrite of a neuron would be visible, but the inner structure of a spherical cell would extend outside

the near field). These results are significant not only for time-resolved studies of light–matter interaction, but also for other fields that would benefit from the ability of a label-free hyperspectral microscopy with sub-wavelength resolution.

To explore the potential of our approach, we deposited an aggregation of silver-coated silicon dioxide particles with typical diameter of 1–7 μm directly onto the surface of a 12 μm thick BBO crystal. The collection of particles contains a number of small cavities and protrusions expected to locally enhance the electric field on a sub-wavelength scale (hot spots) [53,54]. Indeed, these features become apparent, as can be observed in Fig. 4(a), where the peak intensity is pictured. Since each pixel contains a complete electric field waveform, other characteristics of interest such as electric field decay rate or plasmonic couplings could also be analyzed in future measurements of resonant nanostructures. A clear increase in the peak field is observed near small features of the structures in Figs. 4(b) and 4(c). Strikingly, this enhancement is not observed in the standard transmission microscope image at the same location, in case of using the same imaging optics under illumination of the sampling laser, shown in Figs. 4(d) and 4(e). The nature of this enhancement and how the local field information is imprinted on the sampling pulse is investigated through numerical simulation in Supplement 1.

Notably, the features which produce an enhanced electric field contrast share the same orientation; this can be understood based on the polarization sensitivity of the optical properties of small metal objects. Hydrodynamic simulations of these features coupled to the nonlinear medium (see Supplement 1) reveal that the field strength in the medium underneath a metallic rod whose orientation is perpendicular to the direction of the electric field of the infrared is significantly increased, and that this modification of the local field features is accurately reported via EOS.

The corresponding electric field waveform reveals significant differences from that of the pulse transmitted through free space. In this way, the sample structure supplies an automatic reference for studies of the locally enhanced electric field—both are measured simultaneously with perfect synchronicity, as demonstrated by the overlap of the waveforms in the temporal region following the highest field; see Fig. 4(f). This opens the door to studies of the electric field dynamics taking place in plasmonic nanostructures designed for operation in the near-infrared and visible spectral ranges. Additionally, the apparent size of the enhanced features in the image, expected to be substantially sub-wavelength in scale, provides a method of estimating the spatial resolution of the electric field imaging. In Fig. 4(g) the full width at half-maximum of the feature is 1.2 μm, indeed substantially smaller than the shortest input wavelength into the microscope (1.5 μm, with central wavelength 1.9 μm), and below the ≈ 2.4 μm diffraction limit of the 0.4 NA objective.

Since the waveform available for each sub-wavelength pixel can be transformed into the frequency domain, providing amplitude
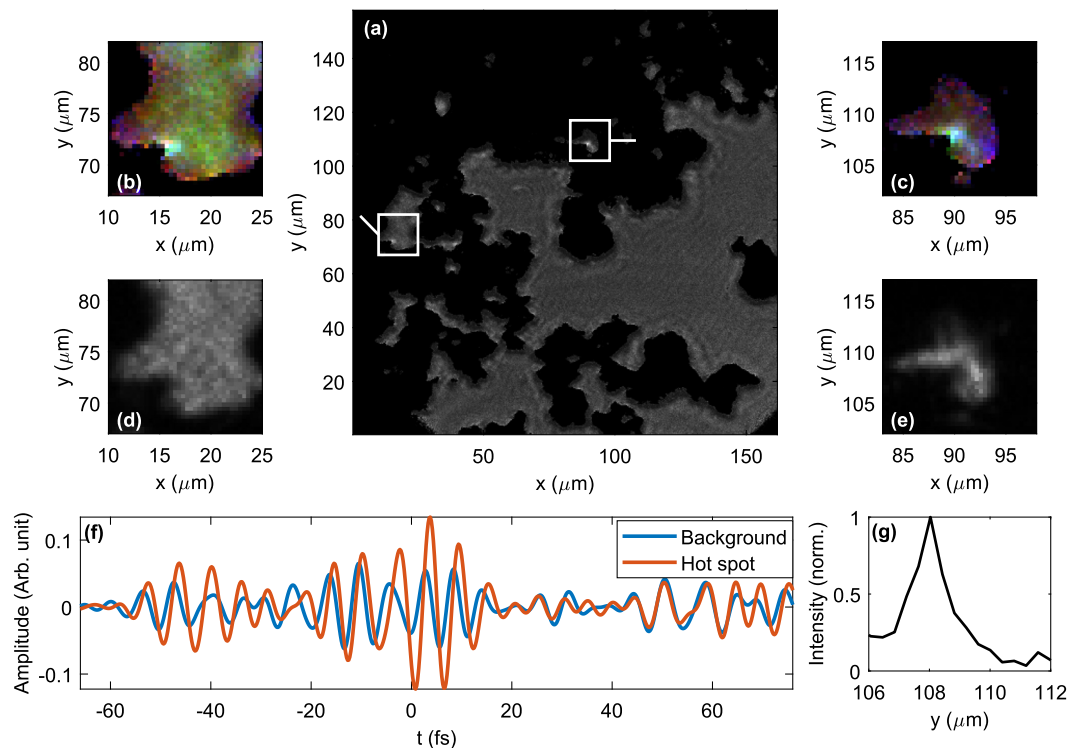
Fig. 4. Sub-wavelength-resolution, time-resolved imaging of the enhanced electric field in the vicinity of aggregated silver-coated fused silica particles. Images were taken with 20×, 0.4 NA objective. (a) A wide-field image showing the peak intensity of each recorded waveform. The brightness of each pixel corresponds to the maximum local intensity of the infrared pulse recorded during the temporal window of the measurement. Note that the apparent sharp outline of black areas is due to gating that sets the field of regions with insufficient sampling signal to zero. (b), (c) Zoomed-in views of the enhanced field strength near sharp corners, shown in false color, where red, green, and blue correspond to 145 THz, 165 THz, and 180 THz, respectively. This makes use of the complete spectral information recorded at each sub-wavelength pixel as an additional enhancement of contrast. (d), (e) Corresponding optical transmission images. These images were obtained by the same imaging optics with only the sampling laser as an illumination source. (f) Electric waveforms at two specific pixels in (c) from the location of the brightest pixel and the relatively unperturbed background. This plot shows the temporal profile of the enhanced field. (g) Lineout of the hotspot in (c), with a FWHM of 1.2 μm.

and phase at each spectral component, the characteristics of assemblies of plasmonic devices may be simultaneously characterized, both in terms of the locations of their resonance frequencies, and the relative phases of their responses to simultaneous excitation. This makes the present imaging geometry a valuable tool for understanding inhomogeneous plasmonic arrays.

5. CONCLUSIONS

In summary, we have demonstrated the direct spatiotemporal imaging of near-infrared electric fields, with sub-wavelength spatial resolution and sub-cycle temporal resolution in a wide-field imaging configuration. We successfully applied it to the characterization of the electric field profiles produced by metalenses. Working in a near-field configuration, the microscopy system produces sub-wavelength spatial resolution in characterizing hot spots in complicated metallic structures, giving direct glimpses into their interaction with rapidly oscillating fields. Accordingly, we foresee that the toolbox of attosecond physics [12,55] can be brought to directly image light–matter interaction, providing a route to spatially and temporally resolved energy transfer in complex systems. This microscopy is expected to have a wide range of applications in nanoscience, optical design and characterization, and wide-field hyperspectral microscopy.

Disclosures. The authors declare no competing interests.

Data availability. All data and image processing codes are available upon request from the corresponding author.

Supplemental document. See Supplement 1 for supporting content.

REFERENCES

1. M. Pastorino, *Microwave Imaging* (Wiley, 2010).
2. D. Saeedkia, ed., *Handbook of THz Technology for Imaging, Sensing and Communications* (Woodhead, 2013).
3. J. Itatani, F. Quéré, G. L. Yudin, M. Y. Ivanov, F. Krausz, and P. B. Corkum, "Attosecond streak camera," Phys. Rev. Lett. **88**, 173903 (2002).
4. E. Goulielmakis, M. Uiberacker, R. Kienberger, A. Baltuska, V. Yakovlev, A. Scrinzi, T. Westerwalbesloh, U. Kleineberg, U. Heinzmann, M. Drescher, and F. Krausz, "Direct measurement of light waves," Science **305**, 1267–1269 (2004).
5. S. B. Park, K. Kim, W. Cho, S. I. Hwang, I. Ivanov, C. H. Nam, and K. T. Kim, "Direct sampling of a light wave in air," Optica **5**, 402–408 (2018).
6. K. T. Kim, C. Zhang, A. D. Shiner, B. E. Schmidt, F. Légaré, D. M. Villeneuve, and P. B. Corkum, "Petahertz optical oscilloscope," Nat. Photonics **7**, 958–962 (2013).
7. P. Carpeggiani, M. Reduzzi, A. Comby, H. Ahmadi, S. Kühn, F. Calegari, M. Nisoli, F. Frassetto, L. Poletto, D. Hoff, J. Ullrich, C. D. Schröter, R. Moshammer, G. G. Paulus, and G. Sansone, "Vectorial optical field reconstruction by attosecond spatial interferometry," Nat. Photonics **11**, 383–389 (2017).
8. S. Ghimire, A. D. DiChiara, E. Sistrunk, P. Agostini, L. F. DiMauro, and D. A. Reis, "Observation of high-order harmonic generation in a bulk crystal," Nat. Phys. **7**, 138–141 (2011).
9. M. Garg, H. Y. Kim, and E. Goulielmakis, "Ultimate waveform reproducibility of extreme-ultraviolet pulses by high-harmonic generation in quartz," Nat. Photonics **12**, 291–296 (2018).
10. S. Ghimire and D. A. Reis, "High-harmonic generation from solids," Nat. Phys. **15**, 10–16 (2019).
11. M. Miranda, F. Silva, L. Neoričić, C. Guo, V. Pervak, M. Canhota, A. S. Silva, Í. J. Sola, R. Romero, P. T. Guerreiro, A. L'Huillier, C. L. Arnold, and H. Crespo, "All-optical measurement of the complete waveform of octave-spanning ultrashort light pulses," Opt. Lett. **44**, 191–194 (2019).
12. S. Sederberg, D. Zimin, S. Keiber, F. Siegrist, M. S. Wismer, V. S. Yakovlev, I. Floss, C. Lemell, J. Burgdörfer, M. Schultze, F. Krausz, and N. Karpowicz, "Attosecond optoelectronic field measurement in solids," Nat. Commun. **11**, 430 (2020).
13. Y. Liu, J. E. Beetar, J. Nesper, S. Gholam-Mirzaei, and M. Chini, "Single-shot measurement of few-cycle optical waveforms on a chip," Nat. Photonics **16**, 109–112 (2022).
14. J. A. Valdmanis, G. Mourou, and C. W. Gabel, "Picosecond electro-optic sampling system," Appl. Phys. Lett. **41**, 211–212 (1982).
15. Q. Wu and X.-C. Zhang, "Free-space electro-optic sampling of terahertz beams," Appl. Phys. Lett. **67**, 3523–3525 (1995).
16. S. Keiber, S. Sederberg, A. Schwarz, M. Trubetskov, V. Pervak, F. Krausz, and N. Karpowicz, "Electro-optic sampling of near-infrared waveforms," Nat. Photonics **10**, 159–162 (2016).
17. E. Ridente, M. Mamaikin, N. Altwaijry, D. Zimin, M. F. Kling, V. Pervak, M. Weidman, F. Krausz, and N. Karpowicz, "Electro-optic characterization of synthesized infrared-visible light fields," Nat. Commun. **13**, 1111 (2022).
18. B. B. Hu and M. C. Nuss, "Imaging with terahertz waves," Opt. Lett. **20**, 1716–1718 (1995).
19. Q. Wu, T. D. Hewitt, and X.-C. Zhang, "Two-dimensional electro-optic imaging of THz beams," Appl. Phys. Lett. **69**, 1026–1028 (1996).
20. Z. G. Lu, P. Campbell, and X.-C. Zhang, "Free-space electro-optic sampling with a high-repetition-rate regenerative amplified laser," Appl. Phys. Lett. **71**, 593–595 (1997).
21. K. Wynne and D. A. Jaroszynski, "Superluminal terahertz pulses," Opt. Lett. **24**, 25–27 (1999).
22. R. M. Koehl, S. Adachi, and K. A. Nelson, "Direct visualization of collective wavepacket dynamics," J. Phys. Chem. A **103**, 10260–10267 (1999).
23. Z. Jiang, X. G. Xu, and X.-C. Zhang, "Improvement of terahertz imaging with a dynamic subtraction technique," Appl. Opt. **39**, 2982–2987 (2000).
24. F. Blanchard, A. Doi, T. Tanaka, H. Hirori, H. Tanaka, Y. Kadoya, and K. Tanaka, "Real-time terahertz near-ELD microscope," Opt. Express **19**, 8277–8284 (2011).
25. F. Blanchard and K. Tanaka, "Improving time and space resolution in electro-optic sampling for near-field terahertz imaging," Opt. Lett. **41**, 4645–4648 (2016).
26. S. Hunsche, M. Koch, I. Brener, and M. C. Nuss, "THz near-field imaging," Opt. Commun. **150**, 22–26 (1998).
27. H. T. Chen, R. Kersting, and G. C. Cho, "Terahertz imaging with nanometer resolution," Appl. Phys. Lett. **83**, 3009–3011 (2003).
28. T. L. Cocker, D. Peller, P. Yu, J. Repp, and R. Huber, "Tracking the ultrafast motion of a single molecule by femtosecond orbital imaging," Nature **539**, 263–267 (2016).
29. M. Porer, J.-M. Ménard, and R. Huber, "Shot noise reduced terahertz detection via spectrally postfiltered electro-optic sampling," Opt. Lett. **39**, 2435–2438 (2014).
30. F. Bonaretti, D. Faccio, M. Clerici, J. Biegert, and P. Di Trapani, "Spatiotemporal amplitude and phase retrieval of Bessel-X pulses using a Hartmann-Shack sensor," Opt. Express **17**, 9804–9809 (2009).
31. B. Alonso, M. Miranda, F. Silva, V. Pervak, J. Rauschenberger, J. S. Román, Í. J. Sola, and H. Crespo, "Characterization of sub-two-cycle pulses from a hollow-core fiber compressor in the spatiotemporal and spatiospectral domains," Appl. Phys. B **112**, 105–114 (2013).
32. M. Miranda, M. Kotur, P. Rudawski, C. Guo, A. Harth, A. L'Huillier, and C. L. Arnold, "Spatiotemporal characterization of ultrashort laser pulses using spatially resolved Fourier transform spectrometry," Opt. Lett. **39**, 5142–5145 (2014).
33. P. Zhu, R. Jafari, T. Jones, and R. Trebino, "Complete measurement of spatiotemporally complex multi-spatial-mode ultrashort pulses from multimode optical fibers using delay-scanned wavelength-multiplexed holography," Opt. Express **25**, 24015–24032 (2017).

34. A. Borot and F. Quéré, "Spatio-spectral metrology at focus of ultrashort lasers: a phase-retrieval approach," Opt. Express **26**, 26444–26461 (2018).

35. N. Yu, P. Genevet, M. A. Kats, F. Aieta, J.-P. Tetienne, F. Capasso, and Z. Gaburro, "Light propagation with phase discontinuities: generalized laws of reflection and refraction," Science **334**, 333–337 (2011).

36. N. Yu and F. Capasso, "Flat optics with designer metasurfaces," Nat. Mater. **13**, 139–150 (2014).

37. S. M. Kamali, E. Arbabi, A. Arbabi, and A. Faraon, "A review of dielectric optical metasurfaces for wavefront control," Nanophotonics **7**, 1041–1068 (2018).

38. W. T. Chen, A. Y. Zhu, J. Sisler, Y.-W. Huang, K. M. A. Yousef, E. Lee, C.-W. Qiu, and F. Capasso, "Broadband achromatic metasurface-refractive optics," Nano Lett. **18**, 7801–7808 (2018).

39. W. T. Chen, A. Y. Zhu, V. Sanjeev, M. Khorasaninejad, Z. Shi, E. Lee, and F. Capasso, "A broadband achromatic metalens for focusing and imaging in the visible," Nat. Nanotechnol. **13**, 220–226 (2018).

40. M. Kempte, U. Stamm, B. Wilhelmi, and W. Rudolph, "Spatial and temporal transformation of femtosecond laser pulses by lenses and lens systems," J. Opt. Soc. Am. B **9**, 1158–1165 (1992).

41. J.-S. Park, S. Zhang, A. She, W. T. Chen, P. Lin, K. M. A. Yousef, J.-X. Cheng, and F. Capasso, "All-glass, large metalens at visible wavelength using deep-ultraviolet projection lithography," Nano Lett. **19**, 8673–8682 (2019).

42. M. Khorasaninejad, W. T. Chen, R. C. Devlin, J. Oh, A. Y. Zhu, and F. Capasso, "Metalenses at visible wavelengths: diffraction-limited focusing and subwavelength resolution imaging," Science **352**, 1190–1194 (2016).

43. W. T. Chen, M. Khorasaninejad, A. Y. Zhu, J. Oh, R. C. Devlin, A. Zaidi, and F. Capasso, "Generation of wavelength-independent subwavelength Bessel beams using metasurfaces," Light Sci. Appl. **6**, e16259 (2017).

44. M. V. Berry, "The adiabatic phase and Pancharatnam's phase for polarized light," J. Mod. Opt. **34**, 1401–1407 (1987).

45. S. Pancharatnam, "Generalized theory of interference and its applications," in *Proceedings of the Indian Academy of Sciences, Section A* (Springer, 1956), pp. 398–417.

46. J. Durnin, J. J. Miceli, and J. H. Eberly, "Diffraction-free beams," Phys. Rev. Lett. **58**, 1499–1501 (1987).

47. Z. Bouchal, J. Wagner, and M. Chlup, "Self-reconstruction of a distorted nondiffracting beam," Opt. Commun. **151**, 207–211 (1998).

48. M. P. Fischer, N. Maccaferri, K. Gallacher, J. Frigerio, G. Pellegrini, D. J. Paul, G. Isella, A. Leitenstorfer, P. Biagioni, and D. Brida, "Field-resolved detection of the temporal response of a single plasmonic antenna in the mid-infrared," Optica **8**, 898–903 (2021).

49. M. Bionta, F. Ritzkowsky, M. Turchetti, Y. Yang, D. Cattozzo Mor, W. P. Putname, F. X. Kärtner, K. K. Berggren, and P. D. Keathley, "On-chip sampling of optical fields with attosecond resolution," Nat. Photonics **15**, 456–460 (2021).

50. A. Bitzer, A. Ortner, H. Merbold, T. Feurer, and M. Walther, "Terahertz near-field microscopy of complementary planar metamaterials: Babinet's principle," Opt. Express **19**, 2537–2545 (2011).

51. A. Bitzer, H. Merbold, A. Thoman, T. Feurer, H. Helm, and M. Walther, "Terahertz near-field imaging of electric and magnetic resonances of a planar metamaterial," Opt. Express **17**, 3826–3834 (2009).

52. I. Pupeza, M. Huber, M. Trubetskov, W. Schweinberger, S. A. Hussain, C. Hofer, K. Fritsch, M. Poetzlberger, L. Vamos, E. Fill, T. Amotchkina, K. V. Kepesidis, A. Apolonski, N. Karpowicz, V. Pervak, O. Pronin, F. Fleischmann, A. Azzeer, M. Žigman, and F. Krausz, "Field-resolved infrared spectroscopy of biological systems," Nature **577**, 52–59 (2020).

53. N. C. J. van der Valk and P. C. M. Planken, "Electro-optic detection of subwavelength terahertz spot sizes in the near field of a metal tip," Appl. Phys. Lett. **81**, 1558–1560 (2002).

54. A. V. Goncharenko, H. C. Chang, and J. K. Wang, "Electric near-field enhancing properties of a finite-size metal conical nano-tip," Ultramicroscopy **107**, 151–157 (2007).

55. A. Sommer, E. M. Bothschafter, S. A. Sato, C. Jakubeit, T. Latka, O. Razskazovskaya, H. Fattahi, M. Jobst, W. Schweinberger, V. Shirvanyan, V. S. Yakovlev, R. Kienberger, K. Yabana, N. Karpowicz, M. Schultze, and F. Krausz, "Attosecond nonlinear polarization and light-matter energy transfer in solids," Nature **534**, 86–90 (2016).